IEEE Access
Multidisciplinary ⋮ Rapid Review ⋮ Open Access Journal

Received 31 March 2026, accepted 14 May 2026, date of publication 22 May 2026, date of current version 1 June 2026.

Digital Object Identifier 10.1109/ACCESS.2026.3696161

RESEARCH ARTICLE

Optimal Droop Control Strategy for Coordinated Voltage Regulation and Power Sharing in Hybrid AC–MTDC Systems

HONGJIN DU, (Graduate Student Member, IEEE), TUANKU BADZLIN HASHFI, (Student Member, IEEE), RASHMI PRASAD, (Member, IEEE), PEDRO P. VERGARA, (Senior Member, IEEE), PETER PALENSKY, (Senior Member, IEEE), AND ALEKSANDRA LEKIĆ, (Senior Member, IEEE)

Department of Electrical Sustainable Energy, Delft University of Technology, 2628 CD Delft, The Netherlands

Corresponding author: Hongjin Du (h.du@tudelft.nl)

ABSTRACT With the growing integration of Modular Multilevel Converters (MMCs) in Multi-Terminal Direct Current (MTDC) transmission systems, there is a growing need for control strategies that balance economic efficiency with robust dynamic performance. This paper presents an enhanced Optimal Power Flow (OPF)-based framework for hybrid AC–MTDC systems, incorporating a novel droop control strategy that jointly coordinates DC-voltage and AC-frequency regulation. By embedding frequency control loops into the MMCs, the method enables system-wide coordination that enhances power sharing and improves resilience under disturbances. The proposed strategy dynamically adjusts converter operating points to minimize generation costs and DC-voltage deviations, balancing economic objectives with system stability. A modified Nordic test system integrated with a four-terminal MTDC grid is used to validate the approach. Optimization is performed using Julia, while the system's dynamic performance is evaluated through electromagnetic transient simulations with the EMTP software. Case studies across multiple scenarios demonstrate that the proposed droop control achieves markedly improved frequency and voltage robustness over active power control, while incurring lower generation costs than the adaptive droop benchmark. The results highlight the ability of the proposed strategy to deliver cost-effective operation without compromising performance, offering a promising solution for the coordinated control of future hybrid AC–DC transmission networks.

INDEX TERMS Droop control, dynamic performance, MMC–MTDC, OPF.

NOMENCLATURE

i, j	Indices for MMC stations, AC buses, or DC buses.
m	Index for submodules in an MMC arm.
M	Modular index.
$U_{\mathrm{SM},m}$	Capacitor voltage of the m-th SM.
N_{total}	Total number of installed submodules per arm.
$N_{\mathrm{active},i}$	Number of active submodules for the i-th MMC.
P_i	Active power at AC bus i (p.u.).
Q_i	Reactive power at AC bus i (p.u.).
U_i	Bus voltage magnitude at AC bus i (p.u.).
δ_i	Phase angle at the i-th PCC (p.u.).
$P_{\mathrm{c},i}$	Active power at the converter AC terminal (p.u.).
$Q_{\mathrm{c},i}$	Reactive power at the converter AC terminal (p.u.).
$U_{\mathrm{c},i}$	AC voltage magnitude at the converter AC terminal (p.u.).
$I_{\mathrm{c},i}$	Converter reactor current magnitude(p.u.).

The associate editor coordinating the review of this manuscript and approving it for publication was Katherine VanDenburgh.

$P_{\text{loss},i}$	Internal power losses of the i-th MMC (p.u.).
a, b, c	Empirical loss coefficients (p.u.).
$f_i, f_{i,\text{ref}}$	Measured frequency and nominal reference frequency (p.u.).
$U_{\text{dc},i}$	Pole-to-ground DC voltage at DC bus i (p.u.).
$U_{\text{dc, ref}}$	DC-voltage reference (p.u.).
$U_{\text{dc, 0}}$	Initial DC-voltage reference (p.u.).
$I_{\text{dc},i}$	DC current flowing toward the DC grid (p.u.).
$P_{\text{dc},i}$	DC power injection into the DC grid (p.u.).
$P_{\text{dc, ref}}$	DC-power reference (p.u.).
$P_{\text{dc, 0}}$	Initial DC-power reference (p.u.).
$Y_{\text{dc},ij}$	Admittance between DC buses i and j (p.u.).
$k_{\text{v}}, k_{\text{f}}$	Adaptive voltage and frequency droop coefficients (p.u.).
k_{droop}	Droop coefficient for the conventional scheme (p.u.).
S_{base}	System power base (100 MVA).

I. INTRODUCTION

Over the past two decades, renewable energy technologies, particularly solar PV and wind power, have advanced remarkably. In 2023, global renewable power capacity additions surged by an estimated 36% to reach 473 GW, marking a record for the 22nd consecutive year. However, integrating such high shares of geographically dispersed RES into utility-scale power systems increasingly stresses existing transmission infrastructure, making the grid a limiting factor for further renewable deployment [1].

To address this, High Voltage Direct Current (HVDC) technology has emerged as a transformative solution for efficient long-distance power transmission and grid stabilization. The successful implementation of HVDC projects worldwide highlights its practicality and potential [2]. Building on the proven point-to-point HVDC links, Multi-Terminal Direct Current (MTDC) systems further expand network flexibility and enable complex power exchange. Concurrently, Modular Multilevel Converters (MMCs) have become the preferred Voltage Source Converter (VSC) technology, owing to their modular design and capacity to independently regulate active and reactive power [3], [4], [5]. These advantages make MMC–MTDC systems particularly suitable for interfacing with weak or passive AC grids, where stable DC-voltage regulation is critical for maintaining real-time power balance and coordinated system performance.

Prior to real-time control, identifying economically efficient and secure steady-state operating points is equally critical for MTDC systems. Recent studies have extended conventional Optimal Power Flow (OPF) formulations to hybrid AC–DC grids, coordinating power injections and DC-voltage levels across multiple terminals [6]. To address scalability and communication constraints, distributed optimization techniques such as Generalized Benders Decomposition (GBD) and the Alternating Direction Method of Multipliers (ADMM) have been incorporated into DC OPF frameworks. These methods facilitate coordinated converter setpoint determination while preserving computational tractability and ensuring reliable system-wide operation [7], [8], [9]. Furthermore, framing secure system operation as an optimization problem has been explored to better account for renewable energy uncertainties and ensure grid reliability [10]. However, OPF-based approaches are inherently formulated for steady-state conditions and are not coupled with the dynamic behavior of converter control systems, leaving no unified framework for guaranteeing DC-voltage regulation under disturbances or varying operating conditions. This gap underscores the need for a control framework that unifies steady-state OPF with dynamic voltage regulation to guarantee reliable MTDC operation.

At present, practical MTDC systems rely primarily on two classical control strategies: master-slave and voltage droop control. Master-slave control achieves high precision in power-sharing but depends heavily on fast communication links, rendering it vulnerable to single-point failures and limiting its scalability. In contrast, voltage droop control uses local measurements of DC voltage and current, enabling decentralized operation without extensive communication infrastructure [11], [12], [13], [14].

Beyond these classical paradigms, advanced strategies have been developed to enhance coordination and system-level performances, such as managing reactive power via electric vehicle participation [15] and cooperative consensus-based distributed DC-voltage control [16]. Although these modern frameworks enhance coordination and post-fault resilience, they introduce algorithmic complexity and still require reliable communication links.

Consequently, decentralized droop control remains the fundamental backbone for autonomous and robust MTDC operation. However, conventional fixed droop strategies remain prone to uneven power sharing, such as converter overloading or under-utilization, thereby limiting the scalability and operational efficiency of MTDC systems [17]. To address these inherent limitations without sacrificing decentralization, recent research has shifted towards adaptive and non-linear droop control frameworks [18], [19], [20]. By dynamically adapting to prevailing grid conditions, these approaches significantly improve both power-sharing precision and DC-voltage robustness.

Furthermore, replacing traditional synchronous generators with low-inertia renewable resources weakens frequency regulation capabilities, leading to steeper rates of change of frequency (RoCoF), deeper frequency nadirs, and prolonged recovery times [21]. Despite these stability risks, most power-flow formulations for VSC-MTDC systems adopt simplified frequency representations, often assuming a constant and spatially uniform AC frequency [22], [23], [24]. For instance, [22] presents a branch-based load-flow approach for hybrid AC–DC microgrids with iterative frequency updates, [23] proposes a coordinated regulation scheme enabling spinning-reserve sharing, and [24] uses power-flow solutions to initialize electromagnetic or harmonic simulations.

These studies typically focus on simplified or small-scale configurations and do not fully capture the dynamics of larger interconnected grids. The influence of converter droop settings and DC grid topology on power sharing is further analyzed in [25], and an analytical tool is proposed to evaluate how droop control parameters affect voltage deviations during both steady-state operation and post-contingency conditions.

Traditional DC-voltage control strategies remain insufficient for capturing the dynamics of large interconnected grids. In practice, active- and reactive- power injections at the point of common coupling (PCC) directly alter the local AC power balance and voltage profile. Through the converter's energy balance, these AC-side dynamics propagate into the DC network and destabilize DC voltage trajectories. While recent multi-terminal coordinated frequency support strategies attempt to address this AC–DC interdependence [26], [27], [28], they typically rely on predefined or heuristic control parameters. Crucially, they lack a comprehensive steady-state optimization framework to dynamically adjust these settings, which is necessary to balance economic efficiency with system-wide stability.

To address these challenges, this paper proposes an enhanced OPF-based droop control strategy considering both voltage and frequency in AC–MTDC systems. Case studies are based on the modified Nordic 32 system, which captures realistic inter-area AC interactions without assuming a uniform frequency. The main contributions of this paper are as follows:

(1) A coordinated droop control strategy is proposed that enables simultaneous regulation of DC voltage and AC frequency by embedding frequency control loops into MMCs, jointly optimizing voltage and frequency droop coefficients to transform each MMC into an active provider of frequency ancillary services.

(2) A hierarchical two-stage OPF framework is developed in which DC voltage stability takes precedence over generation cost minimization, establishing a systematic and verifiable link between steady-state planning and dynamic performance.

(3) The proposed strategy is shown to achieve lower generation costs than adaptive droop control while delivering superior dynamic performance compared to active power control, with sub-second computational time confirming real-time applicability.

(4) The proposed strategy is validated on the modified Nordic 32 system integrated with a four-terminal MTDC grid, a large-scale, realistic test environment capturing interactions among multiple interconnected AC areas without assuming a uniform AC frequency.

The remainder of this paper is organized as follows. The configuration of MMC stations and the conventional voltage droop control scheme are reviewed in Section II. The proposed OPF-based droop control strategy is presented in Section III. The feasibility of the proposed control scheme and its impact on the stability of the test system are verified through simulations in Section IV, and Section V draws conclusions.

II. CONFIGURATION OF MMCS AND CONVENTIONAL VOLTAGE DROOP CONTROL

A. MMC CONFIGURATION AND MODELING

As the most widely adopted type of VSC, MMCs play a pivotal role in large-scale MTDC systems by enabling efficient bidirectional AC–DC power conversion. Figure 1 illustrates a typical four-terminal AC–MTDC transmission system integrated with offshore wind farms.

The fundamental structure of an MMC comprises multiple half-bridge submodules (SMs) connected in series to form arms, which are further combined into legs to form the converter, as shown in Figure 2. Unlike conventional two- or three-level VSCs that rely solely on pulse-width modulation (PWM) for voltage synthesis, an MMC synthesizes its output voltage by inserting or bypassing SMs in each arm, producing a stepped waveform. PWM techniques can also be applied within individual SMs to enhance waveform quality or control performance. The number of active SMs (N_{active}) at any given time determines the synthesized voltage:

$$U_{\text{arm}} = \sum_{m=1}^{N} S_m U_{\text{SM},m}, \tag{1}$$

where $S_m \in \{0, 1\}$ is the switching state of the m-th SM, and $U_{\text{SM},m}$ is its capacitor voltage. The modular index M represents the fraction of SMs engaged in voltage synthesis:

$$M = \frac{N_{\text{active}}}{N_{\text{total}}}. \tag{2}$$

The arm voltage dynamics of the upper and lower arms for phase p are described by:

$$U_{\text{u},p} = \sum_{m=1}^{N} S_{m,\text{u}} U_{\text{SM},m,\text{u}}, \tag{3}$$

$$U_{\text{l},p} = \sum_{m=1}^{N} S_{m,\text{l}} U_{\text{SM},m,\text{l}}, \tag{4}$$

where $S_{m,\text{u}}, S_{m,\text{l}} \in \{0, 1\}$ denote the switching states of the upper and lower arm submodules, respectively. The arm currents are related to the DC- and AC-side currents via:

$$i_{\text{u},p} = \frac{I_{\text{dc}}}{3} + I_{\text{c},p} + \frac{i_{x,p}}{2}, \tag{5}$$

$$i_{\text{l},p} = \frac{I_{\text{dc}}}{3} + I_{\text{c},p} - \frac{i_{x,p}}{2}, \tag{6}$$

where I_{dc} is the total DC current, $I_{\text{c},p}$ is the circulating current, and $i_{x,p}$ is the AC phase current for phase p. These relationships correspond directly to the arm current paths illustrated in Figure 2, where the upper and lower arm inductances L_{arm} govern dynamic current transitions during submodule switching, and C_{dc} denotes the DC-link capacitor connected in parallel with the DC terminals to filter DC-side voltage ripple. By dynamically adjusting the number of inserted submodules N_{active}, MMCs approximate a sinusoidal

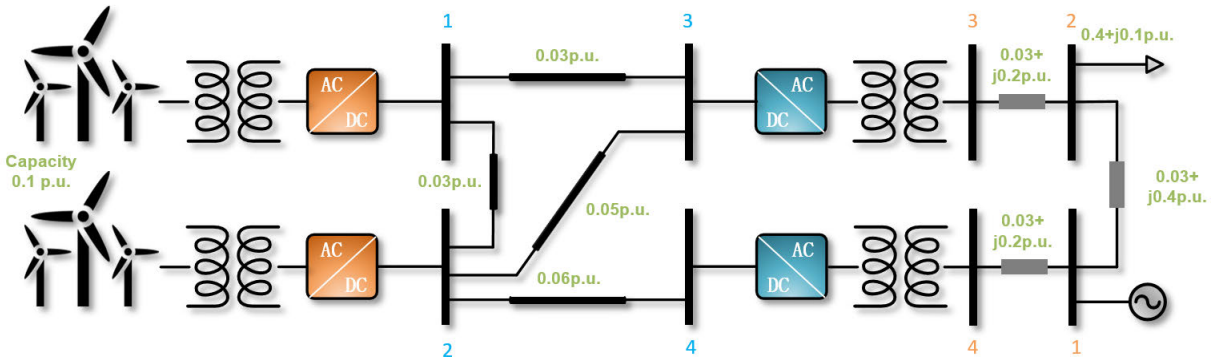

FIGURE 1. Configuration of a 4-terminal AC–MTDC system.

waveform more closely than conventional VSCs, resulting in smoother output voltages, reduced switching losses, and improved voltage scalability. This inherent flexibility allows the MMC to bridge high-level system dispatch and modular hardware execution.

In this work, hardware ratings, such as arm inductance and total installed submodules, are fixed design parameters. The optimal operating points derived from the OPF framework are applied to the outer control loop of each MMC in time-domain simulations, ensuring that the converter's dynamic response remains consistent with the optimization results. Submodule capacitor-voltage balancing is maintained internally by the standard capacitor-voltage balancing algorithm [29], a well-established mechanism in MMC implementations that operates independently of the OPF layer. This mechanism ensures rigorous consistency between steady-state planning and dynamic performance evaluation.

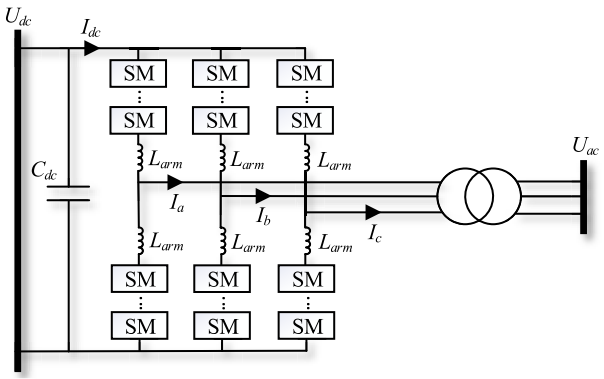

FIGURE 2. Overview of MMC design.

B. CONVENTIONAL VOLTAGE DROOP CONTROL

A typical MMC employs a hierarchical double-loop control structure, as illustrated in Figure 3. The outer loop, often called the secondary control, regulates the DC voltage and active power exchange based on a predefined droop characteristic. This layer enables coordinated system-wide regulation across multiple terminals, while the inner loop comprising current controllers ensures fast tracking of reference values by modulating converter output in real time. In addition, the energy control loop monitors the energies of the submodule capacitors and adjusts the internal circulating current to maintain the desired energy levels, ensuring convergence and stability. Specifically, the circulating-current control regulates the DC-side converter current, which is ideally pure DC, by managing the charging and discharging of the upper and lower arm capacitors. The reference circulating current is derived from the aggregate energy difference between the arms, maintaining the sum of capacitor voltages at the target level, typically equal to DC voltage [29], [30]. The fundamentals of energy and circulating current dynamics can be analyzed from the DC-side loop. According to Kirchhoff's voltage law (KVL):

$$U_{\mathrm{dc}} = (U_{\mathrm{l},p} + U_{\mathrm{u},p}) + 2L\frac{dI_{\mathrm{c},p}}{dt} + 2RI_{\mathrm{c},p}, \tag{7}$$

where U_{dc} is the instantaneous DC-link voltage, $U_{\mathrm{u},p}$ and $U_{\mathrm{l},p}$ denote the upper and lower arm voltages, L and R are the arm inductance and resistance, respectively, and $I_{\mathrm{c},p}$ is the circulating current at each phase.

The total energy stored in the upper and lower arms determines the quality of the internal circulating current in the MMC. The instantaneous arm energies are given by:

$$W_{\mathrm{u},p} = \frac{1}{2}C_{\mathrm{eqv}}\sum_{n=1}^{N}U_{\mathrm{c,u},n,p}^2 \approx \frac{C_{\mathrm{eqv}}}{2N}\left(\sum_{n=1}^{N}U_{\mathrm{c,u},n,p}\right)^2, \tag{8a}$$

$$W_{\mathrm{l},p} = \frac{1}{2}C_{\mathrm{eqv}}\sum_{n=1}^{N}U_{\mathrm{c,l},n,p}^2 \approx \frac{C_{\mathrm{eqv}}}{2N}\left(\sum_{n=1}^{N}U_{\mathrm{c,l},n,p}\right)^2, \tag{8b}$$

where C_{eqv} is the equivalent capacitance, and $U_{\mathrm{c,u},n,p}$ and $U_{\mathrm{c,l},n,p}$ represent the capacitor voltages of the SMs in the upper and lower arms, respectively. It is assumed that the SM voltages are tightly balanced by the internal high-frequency balancing control and the circulating-current suppression control (CCSC). This ensures that individual SM voltage deviations remain negligible relative to the total

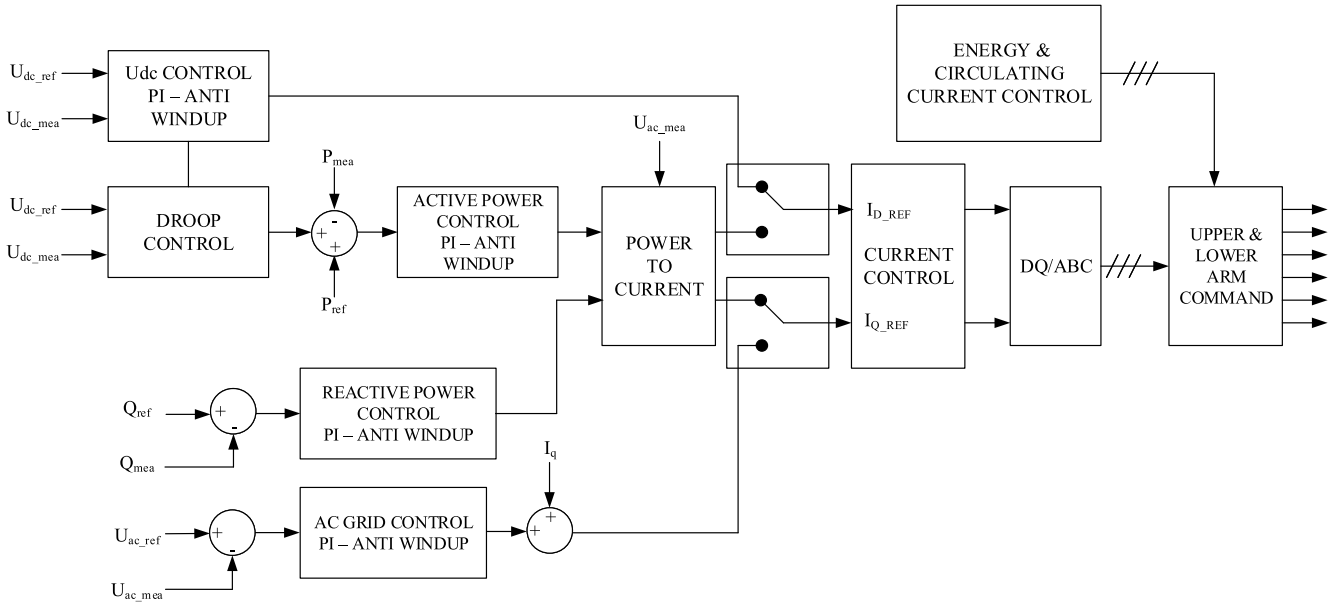

FIGURE 3. MMC operation diagram.

arm voltage, even during disturbances. Consequently, the equivalent continuous model in (8a)–(8b) provides a highly accurate approximation for system-level stability and energy analysis without requiring detailed tracking of individual SM states.

Defining the aggregate and differential arm energies as $W_\Sigma = W_u + W_l$ and $W_\Delta = W_u - W_l$, the corresponding energy balance equations for one phase of an ideal, lossless MMC are obtained as:

$$\frac{dW_\Sigma}{dt} = U_{dc} I_c - U_x I_x, \tag{9a}$$

$$\frac{dW_\Delta}{dt} = U_x I_c - \frac{U_{dc}}{2} I_x, \tag{9b}$$

where U_x is the AC phase voltage. These relationships indicate that the average energy of both arms is primarily governed by the power exchange between the DC and AC sides via the circulating current.

Droop control enables decentralized power sharing and voltage regulation without requiring extensive communication infrastructure. The active power injection at the DC side of the i-th converter can be described by the droop equation:

$$P_{dc,i} - P_{dc,0} + 1/k_{droop}\left(U_{dc,i} - U_{dc,0}\right) = 0, \tag{10}$$

where k_{droop} denotes the droop coefficient; $P_{dc,i}$ and $P_{dc,0}$ are the actual and reference power injected into the DC grid; and $U_{dc,i}$ and $U_{dc,0}$ represent the actual and reference voltage used in the droop control law, respectively.

In an ideal lossless MTDC grid, power imbalances arising from fluctuations or disturbances are naturally distributed among participating VSC stations in proportion to their droop gains. This characteristic offers a simple yet powerful means for voltage regulation and power sharing. Consequently, operators can fine-tune k_{droop} to govern each converter's contribution to voltage support following disturbances. However, while smaller droop coefficients increase converter participation and responsiveness, overly aggressive settings may induce instability or oscillations owing to tightly coupled control loops.

The selection of k_{droop} is therefore critical, as it governs both steady-state power distribution and dynamic response, directly affecting stability margins. In practical scenarios, converters operate under diverse conditions, including varying inertia, load profiles, and system topologies. These complexities necessitate a robust and flexible control design.

To address these challenges, this paper proposes a coordinated droop control strategy that enhances the conventional approach by simultaneously regulating DC voltage and stabilizing AC frequency. This approach dynamically adjusts droop settings in accordance with operating conditions, thereby improving post-disturbance recovery and ensuring smoother transitions to new steady states. By embedding system-level optimization into the control framework, the proposed strategy achieves effective voltage regulation, fair power-sharing, and improved dynamic stability, with decentralized droop-based control that minimizes reliance on centralized communication. Further details are discussed in the following section.

III. PROPOSED CONTROL FRAMEWORK

Traditional droop strategies often neglect the coupling between voltage regulation and power dispatch, particularly under varying operating conditions. To overcome these limitations, we develop a coordinated control framework and an optimal droop-based control model grounded in the AC/DC power-flow formulation, originally introduced in [31]. This integration enables converter control actions to

be directly embedded within the steady-state optimization process, yielding more accurate and realistic operating points for the hybrid power system.

A. FORMULATION OF THE OPTIMIZATION PROBLEM

The proposed optimization problem is formulated as a two-stage process aimed at minimizing both generation cost and DC voltage deviation. The corresponding objective functions are defined as:

$$Obj_1 = \min \sum_{i=1}^{G} (\alpha_i P_{\mathrm{G},i}^2 + \beta_i P_{\mathrm{G},i} + \gamma_i), \tag{11}$$

$$Obj_2 = \min \sum_{j=1}^{D} (U_{\mathrm{dc},j} - U_{\mathrm{rated},j})^2, \tag{12}$$

where $P_{\mathrm{G},i}$ denotes the active power generation at generator i in set G, while α_i, β_i, and γ_i are the corresponding cost coefficients. Furthermore, $U_{\mathrm{dc},j}$ and $U_{\mathrm{rated},j}$ represent the actual and rated DC voltages at DC node j in set D, respectively.

Conventional OPF formulations typically prioritize generation-cost minimization (Obj_1) to achieve optimal steady-state economic performance. However, the unique capability of MMCs to participate in power sharing by dynamically adjusting active-power injections in response to DC-voltage variations requires explicit consideration. Therefore, the proposed strategy incorporates a secondary objective (Obj_2) to minimize DC-voltage deviations. This integrated approach actively regulates the DC voltage toward its nominal level under various operating conditions, thereby improving the system's dynamic response. Crucially, the proposed formulation does not employ a conventional multi-objective optimization framework. Instead, it utilizes a hierarchical structure where DC-voltage stability takes precedence over cost minimization, particularly during dynamic operating conditions.

Accordingly, a sequential optimization is formulated: Stage 1 solves a standard AC–DC OPF to minimize generation costs (Obj_1), yielding system setpoints that are subsequently fixed in Stage 2, where a second OPF determines the optimal droop coefficients by minimizing DC voltage deviations (Obj_2).

A detailed description of this two-stage framework is further elaborated in Section III-B via Figure 5.

For the AC network, the power flow equations are expressed as:

$$P_i = U_i \sum_{j=1}^{n} U_j [G_{ij} cos(\delta_i - \delta_j) + B_{ij} sin(\delta_i - \delta_j)], \tag{13}$$

$$Q_i = U_i \sum_{j=1}^{n} U_j [G_{ij} sin(\delta_i - \delta_j) - B_{ij} cos(\delta_i - \delta_j)], \tag{14}$$

$$P_{\mathrm{G},i} - P_{\mathrm{D},i} - P_i = 0, \quad Q_{\mathrm{G},i} - Q_{\mathrm{D},i} - Q_i = 0, \tag{15}$$

where P_i and Q_i are the active and reactive power at AC bus i, $P_{\mathrm{D},i}$ and $Q_{\mathrm{D},i}$ are the corresponding demands, and $P_{\mathrm{G},i}$ and $Q_{\mathrm{G},i}$ represent the generated powers. U_i is the bus voltage magnitude, G_{ij} and B_{ij} are the conductance and susceptance between AC buses i and j, and δ_i and δ_j are the voltage phase angles.

The MTDC system is modeled as a symmetrical bipolar configuration, where $U_{\mathrm{dc},i}$ represents the pole-to-ground voltage. The positive direction of the DC current $I_{\mathrm{dc},i}$ is defined as the current flowing from the converter toward the DC grid. Consequently, the DC grid is modeled using the following set of equations:

$$I_{\mathrm{dc},i} = \sum_{j=1, j\neq i}^{n} Y_{\mathrm{dc},ij} (U_{\mathrm{dc},i} - U_{\mathrm{dc},j}), \tag{16}$$

$$P_{\mathrm{dc},i} = 2 U_{\mathrm{dc},i} I_{\mathrm{dc},i}, \tag{17}$$

where $Y_{\mathrm{dc},ij}$ is the admittance between DC buses i and j.

To maintain mathematical consistency and simplify the dimensional analysis, all system variables are expressed per-unit on a common power base S_{base}. Specifically, for the i-th converter station, the power losses $P_{\mathrm{loss},i}$, comprising no-load, linear, and quadratic losses, and the complex power balance at the AC terminal are modeled as follows:

$$P_{\mathrm{loss},i} = a + b I_{\mathrm{c},i} + c I_{\mathrm{c},i}^2, \tag{18}$$

$$P_{\mathrm{c},i}^2 + Q_{\mathrm{c},i}^2 - (U_{\mathrm{c},i} I_{\mathrm{c},i})^2 = 0, \tag{19}$$

$$P_{\mathrm{c},i} = U_{\mathrm{c},i} I_{\mathrm{c},i} \cos\phi_i, \tag{20}$$

$$Q_{\mathrm{c},i} = U_{\mathrm{c},i} I_{\mathrm{c},i} \sin\phi_i, \tag{21}$$

where a, b, and c are the empirical loss coefficients listed in Table 1; $U_{\mathrm{c},i}$ and $I_{\mathrm{c},i}$ are the voltage and current on the AC-side, respectively, and ϕ_i is the power factor angle at the i-th PCC.

To ensure a consistent power flow convention, the power balance across the converter is maintained as:

$$P_{\mathrm{c},i} = P_{\mathrm{dc},i} + P_{\mathrm{loss},i}. \tag{22}$$

This formulation ensures that the energy conservation law is strictly followed across the AC and DC sides of the MMC.

TABLE 1. VSC power loss coefficients (p.u., S_{base} = 100 MVA) [31].

	a	b	c
Rectifier	0.011	0.003	0.004
Inverter	0.011	0.003	0.007

Finally, a set of operational constraints is applied to guarantee the physical feasibility and secure operation of the system:

$$U_i^{min} \le U_i \le U_i^{max}, \quad \delta_i^{min} \le \delta_i \le \delta_i^{max}, \tag{23}$$

$$P_{\mathrm{G},i}^{min} \le P_{\mathrm{G},i} \le P_{\mathrm{G},i}^{max}, \quad Q_{\mathrm{G},i}^{min} \le Q_{\mathrm{G},i} \le Q_{\mathrm{G},i}^{max}, \tag{24}$$

$$P_{\mathrm{dc},i}^{min} \le P_{\mathrm{dc},i} \le P_{\mathrm{dc},i}^{max}. \tag{25}$$

These constraints enforce acceptable voltage magnitudes and phase angles at AC buses, along with active- and reactive-power limits of generators. On the DC side,

converter injection limits are imposed to reflect the technical boundaries of power exchange between AC and DC grids. Together, these bounds ensure that the OPF yields solutions that are both mathematically optimal and practically implementable in real-time simulations.

B. PROPOSED DROOP CONTROL STRATEGY

This section introduces the proposed droop control strategy, which is integrated into the optimization process described previously. Given the inherent limitations of AC systems interfaced with DC grids, incorporating frequency regulation into the OPF is essential, particularly for weak AC systems. This can be achieved by incorporating a frequency regulating block into the outer control loop of the d-q control system, replacing the conventional DC voltage controller, which is shown in Figure 4. The output of the frequency controller is combined with the voltage droop result, while the ''Choice regulation'' blocks are responsible for selecting or weighting these outputs, which are then summed to produce the reference current. This weighted summation directly corresponds to the additive structure of Equation (26), where the droop coefficients k_v and k_f serve as the weighting factors governing the relative contribution of the voltage and frequency regulation channels, respectively. Notably, the frequency controller does not alter the voltage droop coefficients; rather, it acts as a supplementary channel to the voltage controller, ensuring that the PCC frequency tracks its reference. In this study, the focus shifts from the system's average frequency to the frequency at the PCC points between the AC system and the converters. This localized perspective enables a more precise analysis of AC–DC interactions, where frequency deviations directly drive power-sharing decisions through the converter's droop control mechanism.

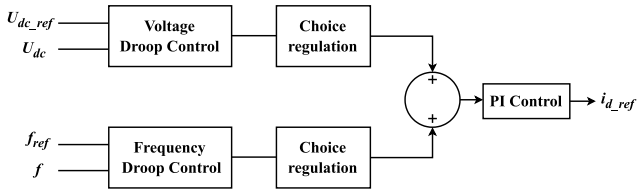

FIGURE 4. Voltage-frequency control in the outer control loop of the d-q control system.

Building on our previous work in [32], which introduced an OPF-based voltage droop control strategy assuming a constant and uniform frequency, this paper proposes an optimized framework that explicitly integrates frequency regulation into the hybrid AC–MTDC grid. This extension is non-trivial as it requires managing the complex interdependencies between DC voltage stability and AC grid inertia within a steady-state OPF formulation. By treating frequency response as an optimizable control variable, the proposed framework elevates the MMC from a passive power-flow follower to an active provider of ancillary services. This coordinated approach aims to improve multi-terminal power

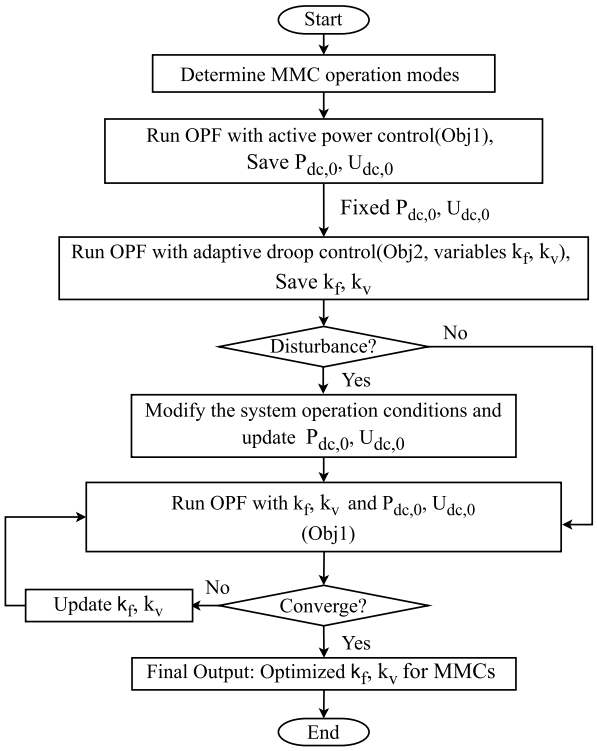

FIGURE 5. Flowchart of the proposed strategy.

sharing and ensure robust stability across both AC and DC domains under severe disturbances, particularly in low-inertia scenarios. Furthermore, the system's dynamic performance is now evaluated through electromagnetic transient simulations using EMTP software, verifying the dynamic resilience of the strategy.

The flowchart of the proposed strategy is illustrated in Figure 5, which is implemented via a co-simulation framework between Julia and EMTP. The optimization is performed in the Julia environment, which leverages high-performance solvers to determine the optimal droop coefficients. The results are then dispatched to the secondary controller in EMTP.

The process begins with the operation of MMCs in active power control mode, aimed at minimizing generation cost (Obj_1). This step determines the active power and voltage set points, $P_{dc,0}$ and $U_{dc,0}$ at the DC buses, which are used as reference values for the droop control. In the second stage, the control shifts to adaptive droop mode, where the frequency and voltage droop coefficients k_v and k_f are treated as variables with the goal of minimizing DC voltage deviation (Obj_2). As noted in [33], frequent adjustments of droop coefficients can potentially impact the stability of the AC–DC system, possibly causing undesirable interactions between the terminals. To address this issue, droop coefficients are initially set and only updated following disturbances.

After a disturbance, the system's operating conditions are updated through the OPF process. The updated droop

coefficients k_v and k_f, along with the revised active power and voltage set points $P_{dc,0}$ and $U_{dc,0}$, are then used as inputs to the OPF with Obj_1. If the optimization converges, Obj_1 is applied in the final step to update the droop characteristics. Otherwise, the droop coefficients k_v and k_f from the previous conditions are revised, and the final optimization step is repeated. Obj_2 is solved over a feasible region parametrized by the optimal setpoints of Obj_1, ensuring that voltage stability is pursued without violating the generation cost optimality established in Stage 1. If the optimization fails to converge due to extreme contingencies or numerical issues, a fallback strategy is activated. In such cases, the secondary controller maintains the droop coefficients from the last stable operating point or reverts to constant DC voltage control to ensure continuous grid integrity. Specifically, the "Disturbance?" decision block in Figure 5 is triggered only by significant events causing permanent changes to network topology or generation capacity, such as generator tripping or MMC disconnection, which necessitate re-optimization of the droop coefficients k_v and k_f. Minor fluctuations and transient disturbances that do not alter the system topology are handled in real time by the existing optimized droop coefficients without triggering a new OPF calculation.

The governing equation for this process is as follows:

$$P_{dc,i} - P_{dc,ref} + 1/k_v \left(U_{dc,i} - U_{dc,ref}\right) + 1/k_f \left(f_i - f_{i,ref}\right) = 0, \tag{26}$$

where f_i denotes the steady-state frequency at each PCC and $f_{i,ref}$ refers to the nominal reference frequency. Under normal operating conditions, $f_i = f_{i,ref}$, reducing Equation (26) to a pure voltage droop characteristic with no frequency contribution. The frequency term becomes active only following significant disturbances such as generator tripping or MMC disconnection, where f_i represents the post-fault quasi-steady-state frequency after fault clearance but before full frequency recovery. This value serves as a fixed input to the second-stage OPF, where k_f is optimized to determine the sensitivity of the DC power injection to the prevailing frequency deviation, with the goal of minimizing DC voltage deviation under post-disturbance operating conditions.

To explicitly connect the optimization objectives to the MMC control implementation, the mapping between each objective and its corresponding control variables are clarified as follows. In Obj_1, the OPF determines the steady-state setpoints $P_{dc,ref}$ and $U_{dc,ref}$ for each converter. These setpoints are directly applied to the outer control loop of the MMC (Figure 3): $P_{dc,ref}$ serves as the reference for the active power controller (P_{ref} in Figure 3), while $U_{dc,ref}$ initializes the DC voltage droop block (Figure 4). In Obj_2, the droop coefficients k_v and k_f are treated as optimization variables. The resulting optimal k_v and k_f directly parameterize the voltage and frequency droop blocks shown in Figure 4: a DC voltage deviation ($U_{dc,i} - U_{dc,ref}$) produces a power correction scaled by $1/k_v$, while an AC-frequency deviation ($f_i - f_{i,ref}$) at the PCC produces a correction scaled by $1/k_f$. These two signals are combined by the "Choice regulation" block and passed to the PI controller to generate the d-axis current reference $i_{d,ref}$, which ultimately drives the upper and lower arm commands of the MMC through the inner current control loop.

The connection between the droop control law (Equation 26) and the MMC internal state equations (Equations (7)–(9b)) operates through a hierarchical separation of timescales. The inner energy and circulating current control (Equations (7)–(9b)) operates on a fast timescale to maintain submodule capacitor voltage balance, ensuring that the aggregate arm energy W_Σ tracks its reference and that the circulating current I_c remains regulated. The outer droop law then operates on top of this stable inner layer, adjusting the active power setpoint $P_{dc,i}$ in response to system-level voltage and frequency deviations at a slower secondary control timescale. This hierarchical structure ensures that the internal MMC dynamics remain stable while the outer control layer realizes the economically optimal operating points derived from the OPF.

This approach ensures the simultaneous optimization of generation cost minimization and DC voltage stability during dynamic conditions. By integrating both voltage and frequency regulation into the optimization framework, the proposed strategy offers a well-balanced solution that enhances the operation of the AC–MTDC grid in both steady-state conditions and during transient disturbances.

The optimal operating points derived from the OPF (e.g., $U_{dc,i}$, $P_{dc,i}$, k_v, and k_f) are directly dispatched to the secondary controller of each MMC within the EMTP simulation. The submodule-level capacitor voltage balancing is handled internally by the standard balancing algorithm within the MMC control structure, ensuring consistency between the optimal operating point and the converter's dynamic response without requiring explicit submodule-level optimization.

IV. SIMULATION RESULTS

To evaluate the proposed control strategy, a modified Nordic 32 test system integrated with a 4-terminal DC grid and a wind farm, as illustrated in Figure 6, is modeled in MATPOWER format for OPF simulations. The MTDC grid is embedded within the Nordic 32 AC grid by connecting the MMC terminals to four strategically selected AC buses: VSC 1 is connected to bus 4021, VSC 2 to bus 4032, VSC 3 to bus 4042, and VSC 4 to bus 4044. These buses are located in different areas of the Nordic 32 AC system, enabling the DC grid to facilitate inter-area power exchange across geographically separated AC regions. The DC network serves three primary roles in this integrated system: to provide a controllable power transfer path between the four AC connection points, thereby offering an additional degree of freedom for system-wide power flow optimization; (2) to support voltage and frequency regulation in each connected

AC area through the MMC control actions; and (3) to integrate the offshore wind farm, which injects power into the DC grid and redistributes it across the AC network via the MMC terminals. This configuration reflects a realistic deployment scenario for hybrid AC–MTDC transmission systems, where DC grids serve as flexible backbones for bulk power transfer and ancillary service provision.

The case system parameters are sourced from [34] and [35], and the system operates under the Operating Point B settings, where Generators 15, 16, and 18 are each partitioned into two half-capacity units. Compared to the original Operating Point A, this configuration enhances N-1 security and provides greater operational flexibility. Parameters of the test system are listed in Table 2. The computational efficiency was verified on a 12th Gen Intel i7-1265U CPU (1.80 GHz), yielding an average NLP solve time of 0.561 s, confirming that the secondary adaptive droop adjustment is tractable for real-time applications.

Prior to the application of any disturbances, the integrated AC–MTDC dynamic model is rigorously initialized using a converged AC/DC power flow solution. Across all evaluated scenarios, the system operates in a nominal steady state from $t = 0$ s until the onset of the respective contingencies. This steady-state initialization period guarantees that the subsequent dynamic responses are exclusively driven by the applied physical faults, completely free from numerical initialization transients.

Following that, the proposed control strategy is executed, building upon the power model as its cornerstone. The optimization process is implemented in Julia v1.9 using a forked version of the PowerModelsACDC.jl v0.8.0 package [6]. This version has been extended with our specialized coordination logic [36], and the corresponding source code is openly accessible via GitHub to facilitate reproducibility. To facilitate comparative analysis, three dedicated branches are established within the repository: (i) active power control, (ii) adaptive droop control, and (iii) the proposed droop control strategy. Each branch independently formulates and solves the respective optimization problem, generating the operating points for the hybrid AC–MTDC system. The nonlinear optimization problem is solved using the IPOPT v3.14 solver with an optimality tolerance of 10^{-8}, integrated through the JuMP v1.10 modeling framework. Subsequently, the obtained steady-state results are cross-validated in EMTP-rv v4.2 to assess the system's transient performance. The time-domain simulations employ a fixed time step of 20 μs and the Trapezoidal integration method to ensure numerical stability and accuracy under different control strategies [37].

Three representative scenarios are selected to evaluate the performance of the control strategies, each designed based on realistic operational conditions and structured with increasing levels of disturbance severity to test the robustness of the control mechanisms.

1) **Scenario 1:** The system operates under normal operating conditions.

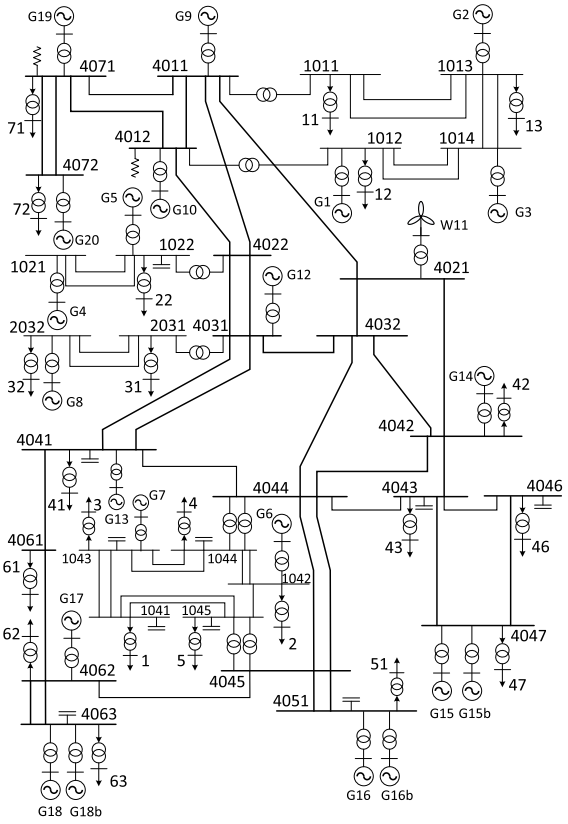

(a) Topology of Nordic 32 test system

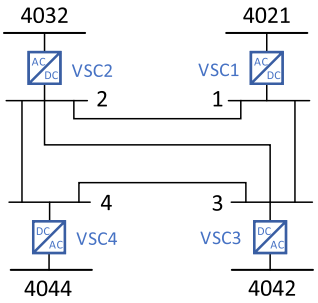

(b) Embedded MTDC system

FIGURE 6. Modified Nordic 32 test system with a 4-terminal MTDC system. VSC 1 connects to AC bus 4021, VSC 2 to bus 4032, VSC 3 to bus 4042, and VSC 4 to bus 4044, enabling inter-area power exchange across the Nordic 32 grid [34], [35].

TABLE 2. Parameters of the integrated AC–MTDC test system.

Category	Parameter	Value
AC Grid (Nordic 32)	Number of AC Buses / Generators	74 / 23
	Total Generation	11,505.9 MW
	Total Load	11,060.0 MW
	Base frequency	50 Hz
DC Grid	DC Voltage Rating	±200 kV
	MMC Rating	480 MVA (each)
	Base voltage	200 kV
	Base Capacity	100 MVA
Wind Farm	Total Installed Capacity	300 MW

2) **Scenario 2:** A fault is initiated at Generator 16, leading to its subsequent disconnection from the system.

3) **Scenario 3:** A fault is applied to MMC 4, resulting in its disconnection from the associated AC grid.

Additionally, three control strategies are implemented and comparatively analyzed to evaluate system performance under different operating conditions, as mentioned previously. These strategies include:

1) **Active power control:** [33], [38] All MMCs operate in constant power control mode, without adaptive response to voltage or frequency fluctuations.
2) **Adaptive droop control:** [33] All MMCs are configured with voltage droop control. Unlike conventional droop control with fixed coefficients, the droop gains (k_v) are adaptively updated based on OPF calculations, allowing them to vary with system operating conditions.
3) **Proposed droop control:** MMCs 1 and 2 are equipped with both voltage and frequency droop control, while MMCs 3 and 4 implement only voltage droop control. Similar to adaptive voltage droop control, the droop coefficients are derived from OPF results.

The per-unit droop coefficients obtained by solving the OPF problem in various scenarios are summarized in Table 3, Table 4, and Table 5, corresponding to the adaptive voltage droop control and the proposed control strategy, respectively. The normalization bases are according to Table 2. Notably, the proposed framework assigns both voltage and frequency regulation to MMCs 1 and 2, while MMCs 3 and 4 operate exclusively in voltage-control mode. This configuration is designed to facilitate a comparative analysis of system performance under different control schemes. The range for the droop coefficients is carefully selected between 0.001 and 1 to maintain the system stability and ensure a balanced trade-off between dynamic response and voltage regulation [39], [40]. For the considered MTDC system, this range represents both a high-sensitivity regulation mode and a near-constant power mode, allowing the optimization layer to minimize the regulation burden on specific stations.

The voltage droop coefficients k_v differ markedly across scenarios for both strategies. Under adaptive voltage droop control, the values for the MMCs are fixed at their limits across all scenarios, which may not be optimal for voltage regulation under dynamic conditions, as it limits the flexibility of the system. In contrast, the proposed droop control allows for more varied values, with the coefficients generally falling within a middle range. This suggests more adaptive and flexible voltage regulation, helping to prevent the system from hitting the control limits and enhancing the ability to respond to system disturbances. In Scenario 2, considering generation loss, certain converters may operate under- or over-loaded compared to their nominal ratings. This affects the droop coefficients as they are adaptively adjusted based on system operating conditions through OPF calculations. As a result, voltage and frequency responses are also modified to maintain system stability. Compared to Scenario 1, Scenario 2 exhibits more uniform or shifted k_v reflecting the changed system conditions. These adaptive adjustments ensure stable voltage and frequency response under varying operating scenarios. In Scenario 3, MMC 2 is assigned a larger share of the load due to the system conditions. However, as shown in Table 4, the droop coefficient for MMC 2 is adjusted accordingly to prevent sustained overloading. The converter may temporarily operate near its rated capacity, but the proposed droop control ensures safe operation.

On the other hand, the frequency droop coefficients k_f under the proposed droop control show significant variation across different scenarios, adjusting the variance of the frequency references. In Scenario 2, where the system experiences a significant fault, the system may initially face instability due to the sudden loss of generation. By reducing k_f, the system enhances its responsiveness to frequency changes, compensating for the disturbance by more actively regulating the frequency to prevent further instability. In Scenario 3, the droop coefficients exhibit distinct adjustments across the remaining MMCs following the outage of MMC 4. Specifically, the droop coefficients k_v and k_f of MMC 1 and MMC 3 increase, indicating a reduction in their power-sharing contribution in response to voltage and frequency deviations. In contrast, MMC 2 shows a decrease in droop coefficients, thereby assuming a larger share of the load compensation. This redistribution of control effort reflects an adaptive rebalancing mechanism within the system, ensuring that the converters respond proportionally based on their capacity and network location. This differentiation helps maintain the support of voltage and frequency while avoiding excessive response from any single converter under constrained operating conditions.

The final optimization results of minimizing generation costs are presented in Table 6. It is observed that active power control generally exhibits superior cost-effectiveness relative to droop control, primarily owing to its capacity to directly optimize power flow without the inherent constraints associated with droop-based regulation. The implementation of droop characteristics can lead to increased generation costs, especially in systems that aim to satisfy multiple operational objectives. However, it is crucial to recognize that droop control strategies offer valuable advantages in enhancing system stability during disturbed conditions by offering reserve margins and supporting robust voltage and frequency regulation.

Notably, Obj_2 is exclusively used within the proposed droop control framework to determine the optimal droop coefficients k_v and k_f, and is not applicable to the benchmark strategies. Furthermore, the Obj_2 values are scenario-specific and depend on the post-disturbance network topology and operating conditions, making cross-scenario comparisons physically inappropriate. The outcome of Obj_2 is therefore reflected in the optimized droop coefficients listed in Tables 4 and 5, and in the DC voltage responses shown in Figures 7, 10, and 13, rather than as a standalone numerical objective value.

TABLE 3. k_v(p.u.) in different scenarios under adaptive voltage droop control.

	Scenario 1	Scenario 2	Scenario 3
MMC 1	1.0000	1.0000	1.0000
MMC 2	1.0000	1.0000	1.0000
MMC 3	1.0000	1.0000	0.0010
MMC 4	0.0010	0.0010	–

TABLE 4. k_v (p.u.) in different scenarios under proposed droop control.

	Scenario 1	Scenario 2	Scenario 3
MMC 1	0.2936	0.4863	0.9999
MMC 2	0.1599	0.4896	0.3594
MMC 3	0.3430	0.9503	0.9999
MMC 4	0.2926	0.9560	–

TABLE 5. k_f (p.u.) in different scenarios under proposed droop control.

	Scenario 1	Scenario 2	Scenario 3
MMC 1	0.5303	0.5065	0.9995
MMC 2	0.5392	0.5052	0.5309

TABLE 6. Objective values ($\times 10^6$ \$/h) in different scenarios.

	Scenario 1	Scenario 2	Scenario 3
Active Power Control	7.1559	7.4725	7.1251
Adaptive Droop Control	7.2828	7.6842	7.2801
Proposed Droop Control	7.2785	7.6835	7.2359

Optimization results demonstrate that the proposed droop control strategy consistently achieves lower generation costs than adaptive droop control (defined as adaptive voltage droop control), highlighting its superior cost-effectiveness. This outcome may be attributed to the adaptive scheme's tendency to modify power references dynamically in response to disturbances, which can lead to suboptimal dispatch decisions and slightly higher generation costs under certain conditions. Alternatively, the proposed method offers a more cost-effective approach by enabling a more gradual response to operational changes. Furthermore, the objective values achieved under the proposed control strategy remain relatively stable across all tested scenarios, demonstrating its ability to consistently maintain cost efficiency.

To validate the effectiveness of the proposed droop control strategy, three predefined scenarios are simulated in EMTP. In Scenarios 2 and 3, system contingencies are introduced at $t_0 = 4.0$ s, with the corresponding faults cleared after a duration of 0.2 seconds. Specifically, Scenario 2 simulates a three-phase short-circuit fault at the terminal of Generator 16, leading to its permanent disconnection from the AC grid by the protection system at $t = 4.2$ s. In Scenario 3, a similar three-phase short-circuit fault is applied to the AC side of MMC 4, resulting in its subsequent blocking and isolation from the system. These disturbances represent a critical loss of generation and a loss of a regulation terminal, respectively, providing a rigorous test for the controller's re-optimization capability under permanent topology changes.

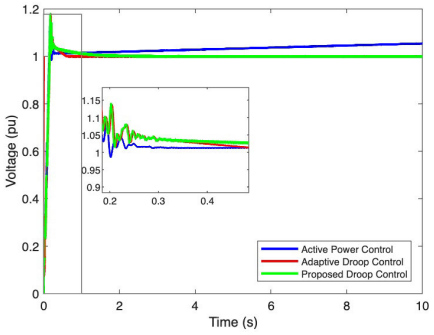

(a) DC voltages at MMC 1

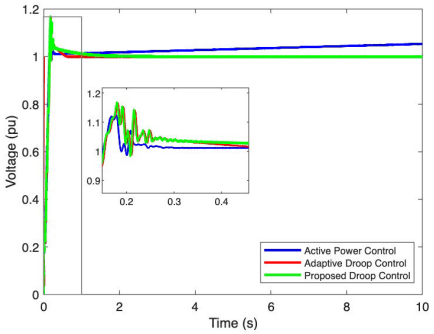

(b) DC voltages at MMC 2

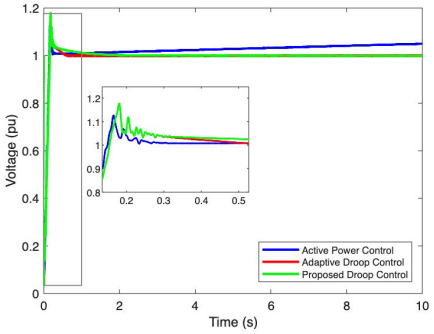

(c) DC voltages at MMC 3

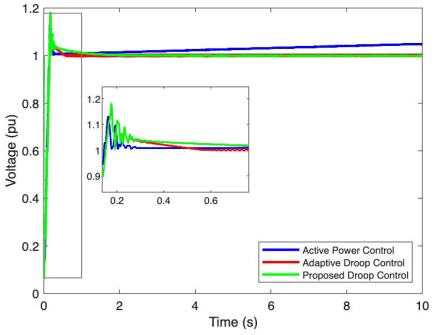

(d) DC voltages at MMC 4

FIGURE 7. DC voltages in Scenario 1 under various control strategies.

For the transient contingencies evaluated in Scenarios 2 and 3, it is important to clarify the sequence of the optimization and parameter updates. During the brief 0.2 s fault duration, the system is governed solely by the primary control layer, utilizing the pre-fault optimal droop parameters to arrest the initial transient. The proposed secondary optimization is inherently designed for the post-fault topological mode. Immediately following the fault clearance and the isolation of the faulted elements, the resulting topology change triggers the execution of the hierarchical OPF. The OPF calculates the new optimal droop coefficients based on the updated post-fault network configuration. Once computed, these updated parameters are dispatched to the MMCs, actively reshaping the converter characteristics to guide the subsequent dynamic recovery and securely transition the system into the new optimal post-fault steady state.

The OPF results are used to initialize the operating points of the test system, and the converter control modes are configured accordingly. The simulation results, as illustrated in Figures 7–14, confirm that the proposed control scheme is capable of effectively mitigating the impact of faults in the AC/DC hybrid system. However, the capability of VSC control alone to restore full system stability remains limited, particularly under severe contingencies. Achieving comprehensive stability may require the coordination of additional compensation components, which is beyond the scope of this study.

In Scenario 1, the system operates under a normal, intact topology without any external faults. The observed dynamic transients are initiated by the activation of the respective control strategies, driving the system from an initial state toward an optimal stationary operating point. As shown in Figure 7, both the adaptive droop control and the proposed method deliver comparable voltage regulation, while active power control fails to maintain voltage stability, exhibiting a continuous voltage rise. In terms of frequency regulation, as shown in Figure 8, the proposed method outperforms the alternatives by effectively damping oscillations and maintaining frequency values closer to the nominal setpoints at the PCC points. The active power responses at the MMC terminals under normal operating conditions are presented in Figure 9. The steady-state terminal powers under active power control settle at nonzero offsets of approximately $+0.7$ p.u. at MMCs 1 and 2 and -0.7 p.u. at MMCs 3 and 4, indicating a persistent mismatch between the fixed power setpoints and the actual power balance requirements of the AC network. This is physically consistent with the DC voltage drift observed in Figure 7.

In contrast, both droop-based strategies drive the terminal powers toward zero, reflecting their ability to adaptively adjust converter injections in response to system conditions. Notably, the zoomed insets reveal that under adaptive droop control, residual oscillations are observable at MMCs 3 and 4, where the terminal power exhibits sustained ripple in steady state, indicating insufficient damping from the voltage-only droop mechanism. The proposed droop control

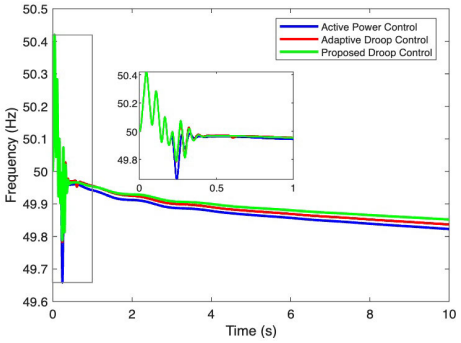

(a) AC frequencies at MMC 1

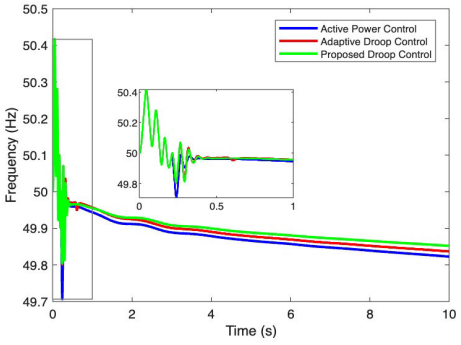

(b) AC frequencies at MMC 2

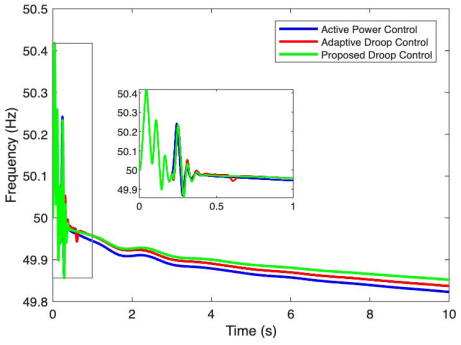

(c) AC frequencies at MMC 3

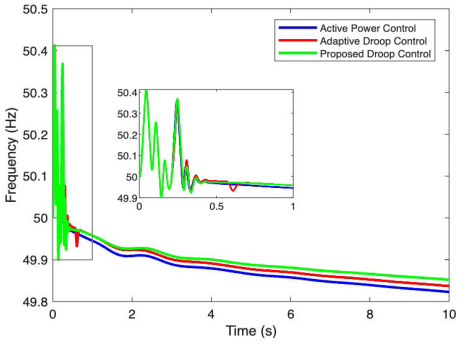

(d) AC frequencies at MMC 4

FIGURE 8. AC frequencies in Scenario 1 under various control strategies.

effectively suppresses these oscillations across all four terminals through the additional frequency correction term

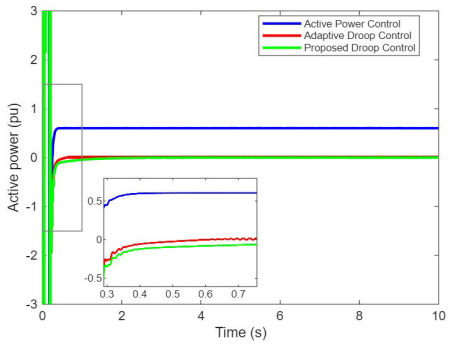

(a) Active power at MMC 1

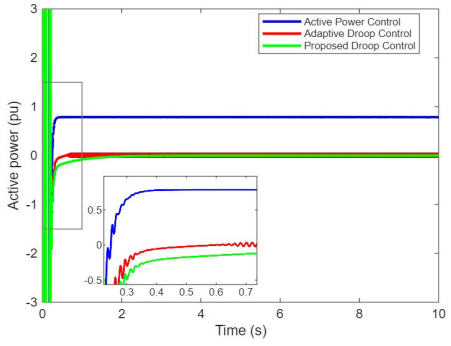

(b) Active power at MMC 2

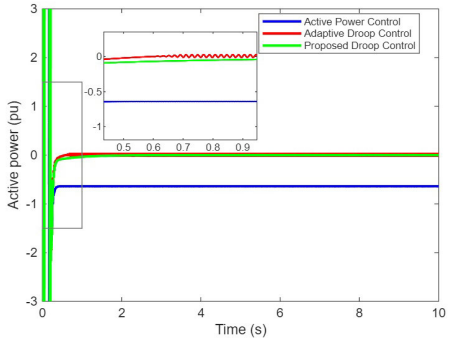

(c) Active power at MMC 3

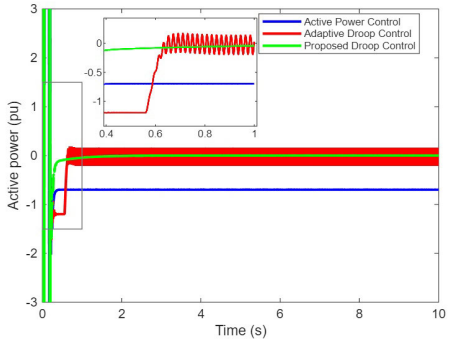

(d) Active power at MMC 4

FIGURE 9. Active powers in Scenario 1 under various control strategies.

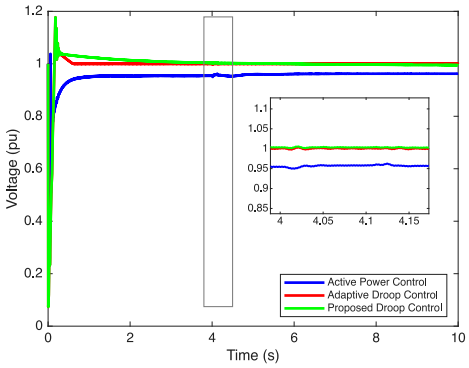

(a) DC voltages at MMC 1

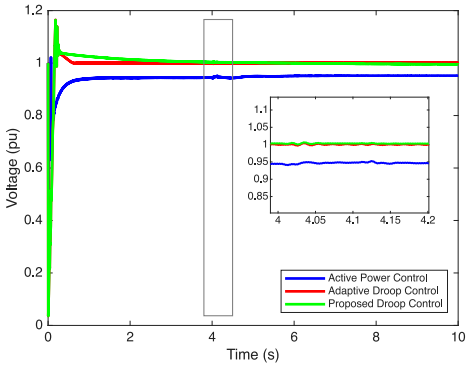

(b) DC voltages at MMC 2

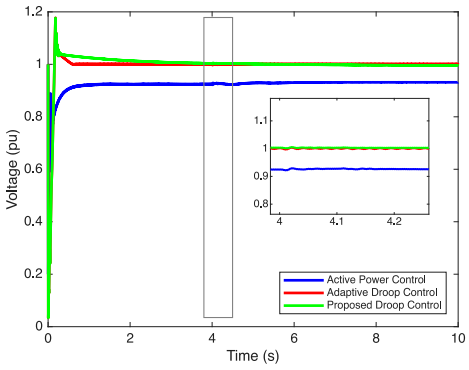

(c) DC voltages at MMC 3

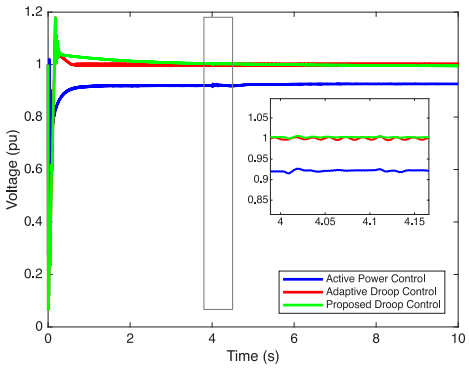

(d) DC voltages at MMC 4

FIGURE 10. DC voltages in Scenario 2 under various control strategies.

$1/k_{\mathrm{f}}(f_i - f_{i,\mathrm{ref}})$ in Equation 26, achieving a smoother and more stable steady-state power profile. This result demonstrates that even when the macro steady-state frequency deviation is near zero, the frequency droop loop dynamically

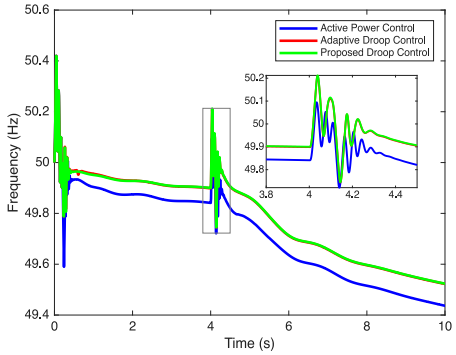

(a) AC frequencies at MMC 1

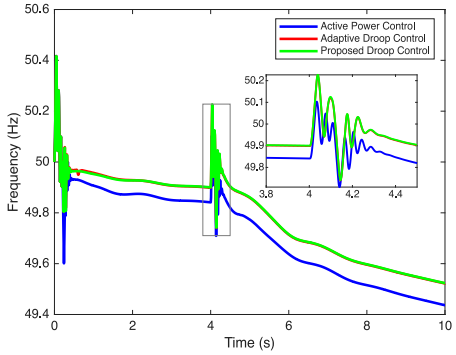

(b) AC frequencies at MMC 2

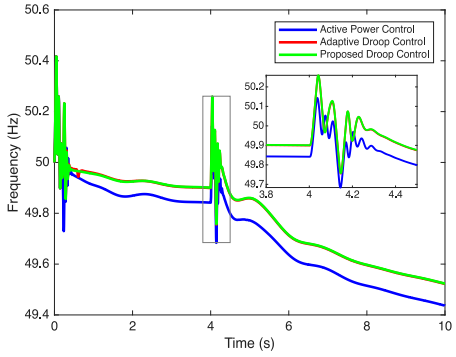

(c) AC frequencies at MMC 3

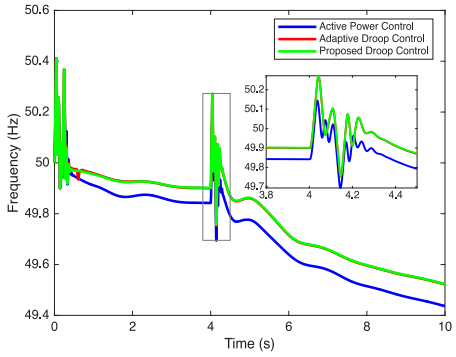

(d) AC frequencies at MMC 4

FIGURE 11. AC frequencies in Scenario 2 under various control strategies.

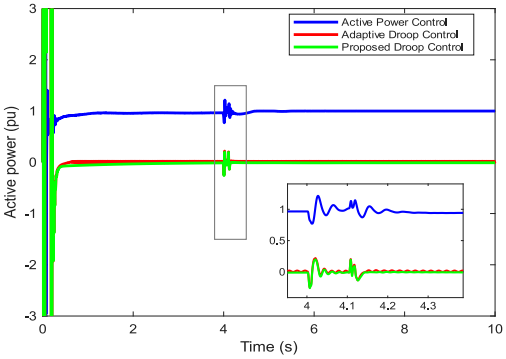

(a) Active power at MMC 1

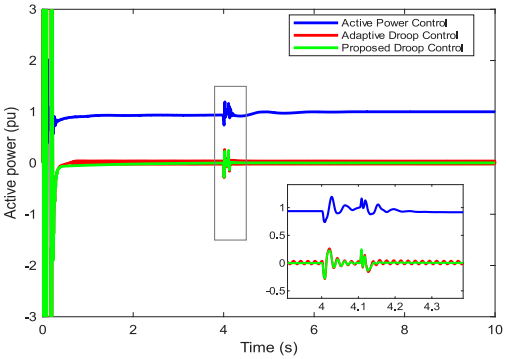

(b) Active power at MMC 2

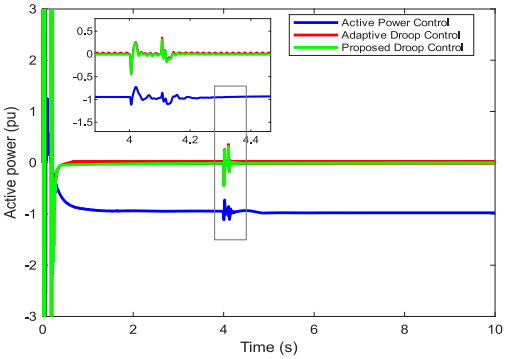

(c) Active power at MMC 3

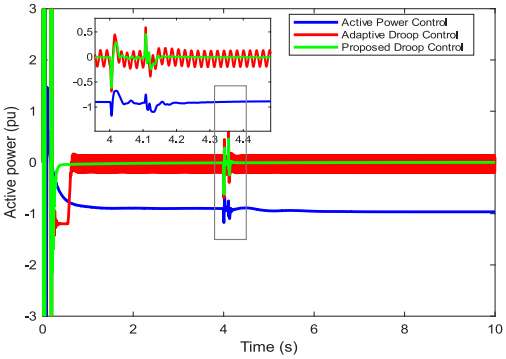

(d) Active power at MMC 4

FIGURE 12. Active powers in Scenario 2 under various control strategies.

contributes to transient damping, thereby improving the overall steady-state power quality by eliminating sustained ripples under routine operational transitions.

In Scenario 2, the disconnection of Generator 16 results in a 630 MW generation deficit. As illustrated in Figure 10, active power control fails to maintain voltage regulation,

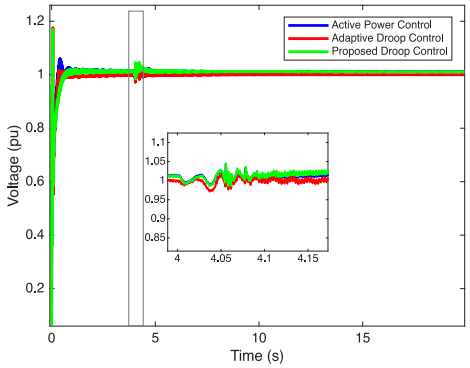

(a) DC voltages at MMC 1

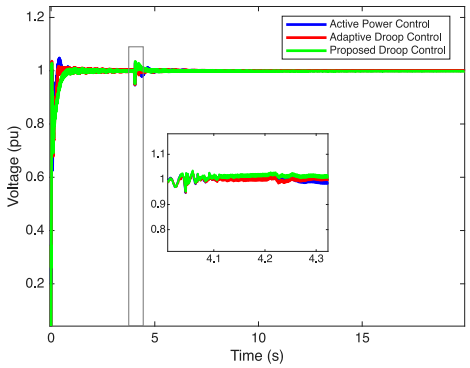

(b) DC voltages at MMC 2

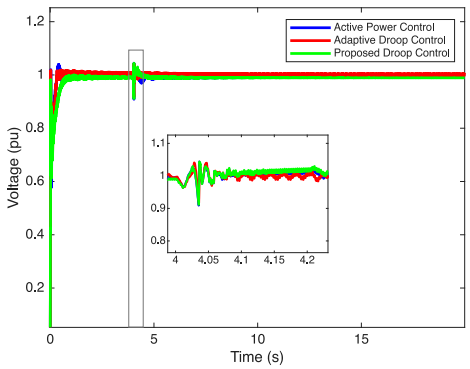

(c) DC voltages at MMC 3

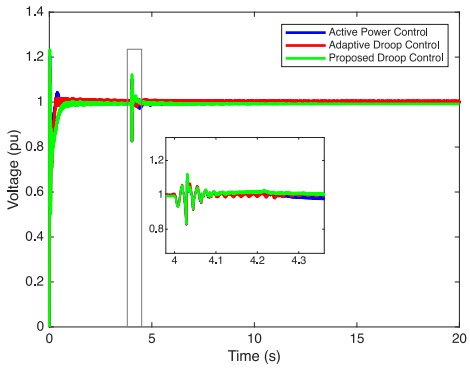

(d) DC voltages at MMC 4

FIGURE 13. DC voltages in Scenario 3 under various control strategies.

causing terminal voltages to plunge to approximately 0.9 p.u. In contrast, the proposed control strategy achieves a more gradual voltage restoration process, restoring the voltages to their nominal values with minimal oscillations. This improved performance can be attributed to the dynamic adaptation of the droop parameters, which enhances the responsiveness of the system under stress. The frequency performance further underscores the limitations of conventional control. As shown in Figure 11, the active power control leads to larger and more prolonged frequency deviations. Meanwhile, the proposed method effectively reduces the magnitude of frequency excursions and provides a slightly faster recovery, thereby contributing to improved frequency stabilization. The active power responses presented in Figure 12 provide complementary evidence of the power-sharing behavior under each control strategy. Under active power control, the terminal powers maintain relatively large steady-state offsets of approximately ±0.8–1 p.u. both before and after the disturbance, which is consistent with the voltage and frequency deviations observed in Figures 10 and 11. Both droop-based strategies maintain terminal power values close to zero throughout the simulation. The primary distinction between the two droop strategies is visible in the zoomed insets: following the fault at $t = 4$ s, the proposed droop control exhibits faster convergence and smaller transient oscillations compared to adaptive droop control, reflecting the additional damping provided by the frequency feedback term.

In Scenario 3, the disconnection of MMC 4 from the AC grid at $t = 4.0$ s introduces a more severe contingency. To facilitate a thorough investigation, the simulation window is extended to 20 seconds. Figure 11 illustrates that all three control strategies exhibit similar voltage performance; however, the proposed strategy restores the voltage to its nominal value more quickly. Under active power control, the system faces difficulties in converging after the contingency, suggesting that the inherent response characteristics of the active power control are insufficient for managing such a large disturbance. In response, MMC 2 is switched to constant-voltage mode to provide voltage support, demonstrating performance comparable to the proposed droop control strategy. This automated transition ensures continuous stability without requiring manual intervention. Furthermore, as illustrated in Figure 14, the proposed control strategy enables faster frequency recovery with reduced oscillations following a disturbance. For instance, under adaptive droop control, the system frequency exhibits sustained oscillations and does not settle until 10 s after the disturbance. The oscillations are also more pronounced compared to the other schemes, indicating the limited damping capability of adaptive droop control under transient conditions. The transient frequency spike ($\approx$ 62 Hz) observed at MMC 4 during the fault is a numerical artifact of the Phase-Locked Loop (PLL). Upon the disconnection of the converter, the PLL input voltage collapses, causing the internal PI controller to drift in the absence of a stable phase reference. As MMC 4 is fully isolated at this stage, this localized measurement anomaly does not influence the adaptive droop

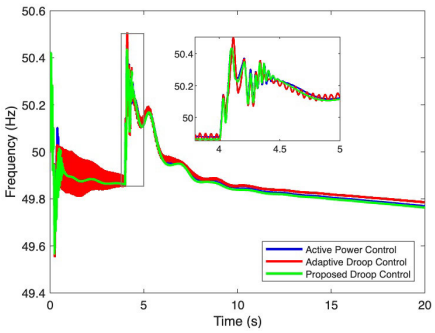

(a) AC frequencies at MMC 1

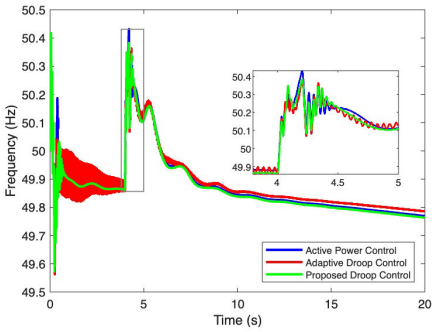

(b) AC frequencies at MMC 2

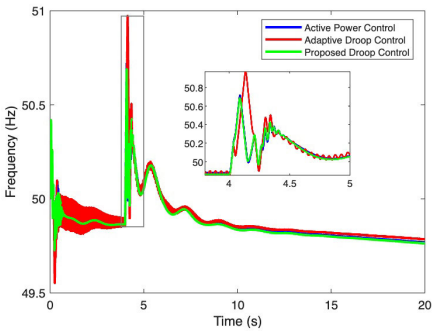

(c) AC frequencies at MMC 3

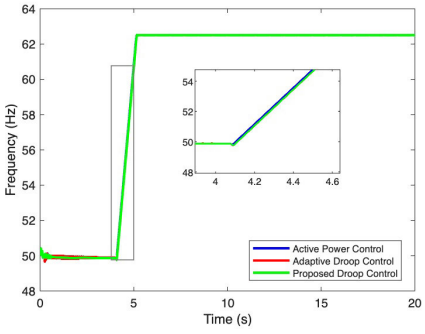

(d) AC frequencies at MMC 4

FIGURE 14. AC frequencies in Scenario 3 under various control strategies.

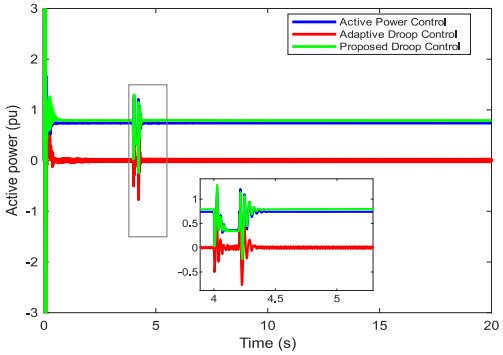

(a) Active power at MMC 1

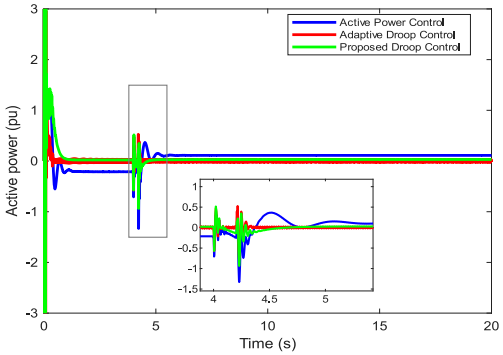

(b) Active power at MMC 2

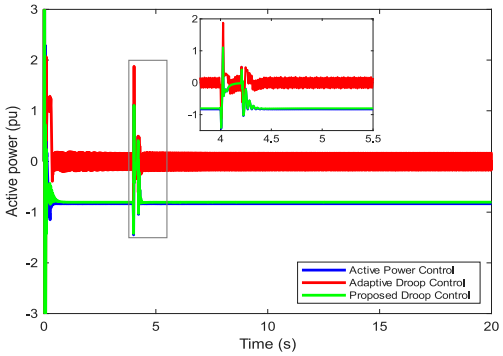

(c) Active power at MMC 3

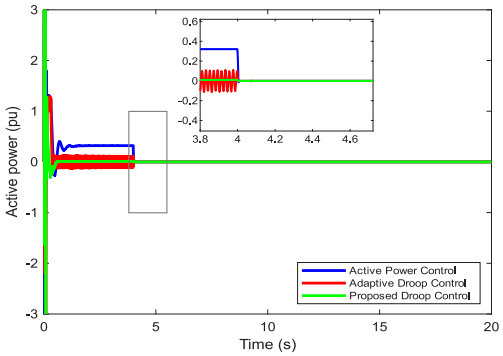

(d) Active power at MMC 4

FIGURE 15. Active powers in Scenario 3 under various control strategies.

response of the remaining system. In practical implementations, a sampling-and-holding or frequency-freezing logic would typically be employed to mask such transients; however, for the purpose of this transparent simulation, the raw PLL output is retained to illustrate the point of disconnection. The active power responses are presented in Figure 15. Under active power control, the terminal powers

TABLE 7. Quantitative dynamic performance metrics (system-wide worst-case).

Scenario	Metric	Active Power	Adaptive Droop	Proposed
Scenario 1	Max DC Vol. Dev. (p.u.)	0.1289	0.1776	0.1789
	Max. Freq. Excursion (Hz)	49.6586	49.7831	49.7881
	Settling Time t_s (s)	> 10	0.6448	0.4227
Scenario 2	Max DC Vol. Dev. (p.u.)	0.0114	0.0055	0.0029
	Max. Freq. Excursion (Hz)	49.6942	49.7524	49.7563
	Settling Time t_s (s)	4.1451	4.1975	4.0281
Scenario 3	Max DC Vol. Dev. (p.u.)	0.8260	0.8275	0.8280
	Max. Freq. Excursion (Hz)	50.7182	50.9724	50.6880
	Settling Time t_s (s)	5.4646	> 10	4.6028

at the remaining MMCs settle at relatively large steady-state offsets, consistent with the voltage and frequency deviations observed in Figures 13 and 14. The power at MMC 4 collapses to zero upon disconnection, as expected. The primary distinction between the two droop strategies is visible in the zoomed insets: the proposed droop control exhibits faster post-contingency convergence and smaller transient oscillations compared to adaptive droop control, reflecting the additional damping provided by the frequency feedback term and the re-optimized droop coefficients k_{v} and k_{f} determined by the second-stage OPF as listed in Tables 4 and 5.

Across all three scenarios, the OPF and time-domain simulation results consistently validate the effectiveness of the proposed strategy in enhancing the stability and operational performance of the hybrid AC–DC system. In a synchronously operated AC system, the steady-state frequency is inherently restored to its nominal value by the generator governors, independent of the MMC control strategy. The contribution of the proposed frequency droop control therefore manifests primarily in the dynamic response, including reduced oscillation amplitude, faster settling time, and improved damping under severe contingencies, as demonstrated in Figures 8, 11, and 14.

To rigorously quantify these dynamic responses, Table 7 summarizes the system-wide worst-case transient metrics for each scenario across the active interconnected grid, including the maximum DC voltage deviation, the extreme frequency excursion (nadir or peak), and the settling time. Compared with conventional active power control and adaptive droop control, the proposed method offers a more balanced and robust solution, particularly in maintaining voltage and frequency regulation during dynamic disturbances, which is a key factor for its practical deployment in real-world power systems. Nonetheless, the results also indicate that VSC-based control alone is insufficient to ensure full system stabilization under extreme contingencies. Therefore, the integration of supplementary compensation mechanisms is necessary to achieve comprehensive and resilient system stability.

V. CONCLUSION

This paper proposes an optimal voltage-frequency droop-based control strategy for hybrid AC–MTDC systems that simultaneously enhances DC-voltage regulation and AC-frequency stability, improving overall power-sharing performance. The proposed strategy embeds a hierarchical OPF-based control framework and demonstrates adaptability and effectiveness in maintaining system stability across various scenarios, validated on a modified Nordic test system integrated with a four-terminal MTDC grid. Compared to conventional active power control and adaptive voltage droop benchmarks, integrating frequency control loops directly into the MMCs delivers a more cost-effective and resilient solution for regulating system voltage and frequency during severe operational disturbances. Furthermore, keeping voltage and frequency tightly bound to their nominal references allows the converters to preserve critical headroom and power margins. This capability is vital for mitigating severe power imbalances during major contingencies without compromising system integrity. Future research will extend this framework by incorporating stochastic uncertainties from high-penetration renewable energy sources, such as offshore wind farms, to enhance the strategy's resilience under highly volatile generation and demand conditions.

REFERENCES

[1] *Renewables 2024 Global Status Report Collection*, REN21, 2024.

[2] C.-K. Kim, V. K. Sood, G.-S. Jang, S.-J. Lim, and S.-J. Lee, "Development of HVDC technology," in *HVDC Transmission: Power Conversion Applications in Power Systems*. Hoboken, NJ, USA: Wiley, 2009, pp. 1–35.

[3] F. Schettler, H. Huang, and N. Christl, "HVDC transmission systems using voltage sourced converters design and applications," in *Proc. Power Eng. Soc. Summer Meeting*, vol. 2, 2000, pp. 715–720.

[4] F. Muhammad, H. Rasheed, D. W. Spier, E. Prieto-Araujo, and O. G. Bellmunt, "Control design and fault handling performance of MMC for MMC-based DC distribution system," *IEEE Access*, vol. 10, pp. 126695–126711, 2022.

[5] J. A. Ansari, C. Liu, and S. A. Khan, "MMC based MTDC grids: A detailed review on issues and challenges for operation, control and protection schemes," *IEEE Access*, vol. 8, pp. 168154–168165, 2020.

[6] H. Ergun, J. Dave, D. Van Hertem, and F. Geth, "Optimal power flow for AC–DC grids: Formulation, convex relaxation, linear approximation, and implementation," *IEEE Trans. Power Syst.*, vol. 34, no. 4, pp. 2980–2990, Jul. 2019.

[7] H. Li, P. P. Vergara, R. Dimitrovski, H. Du, and A. Lekić, "Enhanced AC/DC optimal power flow via nested distributed optimization for AC/VSC-MTDC hybrid power systems," *Int. J. Electr. Power Energy Syst.*, vol. 164, Mar. 2025, Art. no. 110365.

[8] B. Liu, J. Li, H. Ma, and Y. Liu, "Generalized benders decomposition based dynamic optimal power flow considering discrete and continuous decision variables," *IEEE Access*, vol. 8, pp. 194260–194268, 2020.

[9] M. Li, S. Kolouri, and J. Mohammadi, "Learning to optimize distributed optimization: ADMM-based DC-OPF case study," in *Proc. IEEE Power Energy Soc. Gen. Meeting (PESGM)*, Jul. 2023, pp. 1–5.

[10] A. Safari and H. Rahbarimagham, "Flexible-reliable linear AC security constrained unit commitment considering uncertainties and renewable energy sources," *Energy Rep.*, vol. 10, pp. 3814–3825, Nov. 2023.

[11] Z. Li, Y. Li, R. Zhan, Y. He, and X.-P. Zhang, "AC grids characteristics oriented multi-point voltage coordinated control strategy for VSC-MTDC," *IEEE Access*, vol. 7, pp. 7728–7736, 2019.

[12] Y. Wang, Z. Wang, M. Lei, and F. Qiu, "Analysis and control of DC voltage dynamics based on a practical reduced-order model of droop-controlled VSC-MTDC system in DC voltage control timescale," *IEEE Trans. Power Del.*, vol. 39, no. 2, pp. 1031–1039, Apr. 2024.
[13] H. Li, C. Liu, G. Li, and R. Iravani, "An enhanced DC voltage droop-control for the VSC-HVDC grid," *IEEE Trans. Power Syst.*, vol. 32, no. 2, pp. 1520–1527, Mar. 2017.
[14] F. Chen, R. Burgos, D. Boroyevich, J. C. Vasquez, and J. M. Guerrero, "Investigation of nonlinear droop control in DC power distribution systems: Load sharing, voltage regulation, efficiency, and stability," *IEEE Trans. Power Electron.*, vol. 34, no. 10, pp. 9404–9421, Oct. 2019.
[15] A. Safari and H. Rahbarimagham, "An improved control strategy for managing reactive power and reducing capacity of interlinking converters by participating of electric vehicles in hybrid AC/DC microgrids," *IEEE Access*, vol. 13, pp. 17878–17894, 2025.
[16] M. Salman, Y. Li, and J. Xiang, "A distributed consensus-based optimal dispatch control strategy for hybrid AC/DC microgrids," *IEEE Access*, vol. 12, pp. 90997–91010, 2024.
[17] Y. Wang, B. Li, Z. Zhou, Z. Chen, W. Wen, X. Li, and C. Wang, "DC voltage deviation-dependent voltage droop control method for VSC-MTDC systems under large disturbances," *IET Renew. Power Gener.*, vol. 14, no. 5, pp. 891–896, Apr. 2020.
[18] P. Prabhakaran, Y. Goyal, and V. Agarwal, "Novel nonlinear droop control techniques to overcome the load sharing and voltage regulation issues in DC microgrid," *IEEE Trans. Power Electron.*, vol. 33, no. 5, pp. 4477–4487, May 2018.
[19] Y. Wang, F. Qiu, G. Liu, M. Lei, C. Yang, and C. Wang, "Adaptive reference power based voltage droop control for VSC-MTDC systems," *J. Modern Power Syst. Clean Energy*, vol. 11, no. 1, pp. 381–388, Jan. 2023.
[20] Z.-H. Jiang, A. Raza, Y.-D. Ye, M. P. Sahto, G. Raza, M. Haris, M. S. Mastoi, and M. Hassan, "Headroom based adaptive droop control for regulating DC voltage and active power in MTDC grid with integrated renewable energy," *Sci. Rep.*, vol. 16, no. 1, Feb. 2026.
[21] Y. Ye, Y. Qiao, L. Xie, and Z. Lu, "A comprehensive power flow approach for multi-terminal VSC-HVDC system considering cross-regional primary frequency responses," *J. Modern Power Syst. Clean Energy*, vol. 8, no. 2, pp. 238–248, Mar. 2020.
[22] M. E. Nassar, A. A. Hamad, M. M. A. Salama, and E. F. El-Saadany, "A novel load flow algorithm for islanded AC/DC hybrid microgrids," *IEEE Trans. Smart Grid*, vol. 10, no. 2, pp. 1553–1566, Mar. 2019.
[23] H. Xiao, K. Sun, J. Pan, L. Xiao, C. Gan, and Y. Liu, "Coordinated frequency regulation among asynchronous AC grids with an MTDC system," *Int. J. Electr. Power Energy Syst.*, vol. 126, Mar. 2021, Art. no. 106604.
[24] A. Lekić, H. Ergun, and J. Beerten, "Initialisation of a hybrid AC/DC power system for harmonic stability analysis using a power flow formulation," *High Voltage*, vol. 5, no. 5, pp. 534–542, Oct. 2020.
[25] J. Stojković, A. Lekić, and P. Stefanov, "Adaptive control of HVDC links for frequency stability enhancement in low-inertia systems," *Energies*, vol. 13, no. 23, p. 6162, Nov. 2020.
[26] X. Zhao and M. Du, "Multi-terminal coordinated frequency support strategy for alternating current/direct current hybrid voltage source converter-based multi-terminal direct current system," *IEEE Access*, vol. 13, pp. 111997–112010, 2025.
[27] H. Liu and C. Liu, "Frequency regulation of VSC-MTDC system with offshore wind farms," *J. Modern Power Syst. Clean Energy*, vol. 12, no. 1, pp. 275–286, Jan. 2024.
[28] B. E. Ayalew, M. S. E. Moursi, and E. F. El-Saadany, "Enhanced DC voltage and frequency regulation for high voltage AC/DC power grid," *IEEE Trans. Power Syst.*, vol. 39, no. 2, pp. 3374–3388, Mar. 2024.
[29] A. Elsanabary, T. B. Hashfi, S. Mekhilef, M. Seyedmahmoudian, and A. Stojcevski, "Submodule fault-tolerant control based adaptive carrier-PDPWM for modular multilevel converters," *Energy Rep.*, vol. 7, pp. 7288–7296, Nov. 2021.
[30] S. Fan, K. Zhang, J. Xiong, and Y. Xue, "An improved control system for modular multilevel converters with new modulation strategy and voltage balancing control," *IEEE Trans. Power Electron.*, vol. 30, no. 1, pp. 358–371, Jan. 2015.
[31] J. Beerten, S. Cole, and R. Belmans, "A sequential AC/DC power flow algorithm for networks containing multi-terminal VSC HVDC systems," in *Proc. IEEE PES Gen. Meeting*, Jul. 2010, pp. 1–7.
[32] H. Du, R. Prasad, A. Lekić, P. P. Vergara, and P. Palensky, "Enhanced optimal power flow based droop control in MMC-MTDC systems," in *Proc. IEEE PES Innov. Smart Grid Technol. Eur. (ISGT EUROPE)*, Oct. 2024, pp. 1–5.
[33] Y. Zhang, X. Meng, A. M. Shotorbani, and L. Wang, "Minimization of AC–DC grid transmission loss and DC voltage deviation using adaptive droop control and improved AC–DC power flow algorithm," *IEEE Trans. Power Syst.*, vol. 36, no. 1, pp. 744–756, Jan. 2021.
[34] B. Li, Q. Li, Y. Wang, W. Wen, B. Li, and L. Xu, "A novel method to determine droop coefficients of DC voltage control for VSC-MTDC system," *IEEE Trans. Power Del.*, vol. 35, no. 5, pp. 2196–2211, Oct. 2020.
[35] T. Van Cutsem et al., "Test systems for voltage stability analysis and security assessment," PES Power System Stability Subcommittee, Tech. Rep. PES-TR19, Aug. 2015.
[36] H. Du. (2025). *Modified Version of PowerModelsACDC.jl for Customized Optimization Routines*. [Online]. Available: https://github.com/hongjin7/PMACDC-HD
[37] J. Mahseredjian, S. Dennetière, L. Dubé, B. Khodabakhchian, and L. Gérin-Lajoie, "On a new approach for the simulation of transients in power systems," *Electr. Power Syst. Res.*, vol. 77, no. 11, pp. 1514–1520, Sep. 2007.
[38] K. Rouzbehi, A. Miranian, A. Luna, and P. Rodriguez, "DC voltage control and power sharing in multiterminal DC grids based on optimal DC power flow and voltage-droop strategy," *IEEE J. Emerg. Sel. Topics Power Electron.*, vol. 2, no. 4, pp. 1171–1180, Dec. 2014.
[39] F. Zhang and Q. Li, "Methodology of calculating droop coefficients for stabilising DC voltage in VSC-MTDC system against disturbances," *IET Gener., Transmiss. Distrib.*, vol. 13, no. 4, pp. 521–535, Feb. 2019.
[40] *Guide for the Development of Models for*, CIGRE Working Group B4.57, Paris, France, Oct. 2014.

HONGJIN DU (Graduate Student Member, IEEE) received the B.Sc. and M.Sc. degrees in electrical engineering from Northeast Electric Power University (NEEPU), China, in 2015 and 2018, respectively. She is currently pursuing the Ph.D. degree in electrical engineering with Delft University of Technology (TU Delft), The Netherlands.

She was an Electrical Engineer with China Huadian Electric Power Research Institute (CHDER), from 2018 to 2022. Her primary research interests include coordinated optimal control for hybrid AC–MTDC power systems and power system analysis.

TUANKU BADZLIN HASHFI (Student Member, IEEE) received the B.Eng. degree (Hons.) in electrical and electronics engineering from the National University of Malaysia, Selangor, Malaysia, in 2015, and the M.Eng.Sc. degree from the University of Malaya, Kuala Lumpur, Malaysia, in 2021. He is currently pursuing the Ph.D. degree in electrical engineering with TU Delft, The Netherlands.

He has worked on research projects related to DC/DC converters, AC/DC converters, and modular multilevel converters (MMC), including their control strategies. His research interests include power electronics, converter design, and the control of MMC systems.

RASHMI PRASAD (Member, IEEE) received the B.Eng. degree in electrical and electronics engineering from the Silicon Institute of Technology, India, in 2014, and the M.Sc. and Ph.D. degrees in mine electrical engineering from Indian Institutes of Technology, India, in 2017 and 2023, respectively.

She was a Postdoctoral Researcher with TU Delft, from 2023 to 2024. She is currently an Assistant Professor with the National Institute of Technology Rourkela, India. Her research interests include modeling and analysis in power system dynamics, control, and renewable generation integration.

PEDRO P. VERGARA (Senior Member, IEEE) received the B.Sc. degree in electrical engineering from the Universidad Industrial de Santander (UIS), Colombia, the M.Sc. degree in electrical engineering from the State University of Campinas (UNICAMP), Brazil, and the double Ph.D. degree in electrical engineering from UNICAMP and the University of Southern Denmark (SDU), Denmark.

His postdoctoral work was conducted with the Electrical Energy Systems Group, Eindhoven University of Technology (TU/e), The Netherlands. He is currently an Associate Professor with the Intelligent Electrical Power Grids Group, TU Delft, The Netherlands.

PETER PALENSKY (Senior Member, IEEE) received the Ph.D. degree from Vienna University of Technology, Austria.

He is currently a Full Professor of intelligent electric power grids and the Head of the Electrical Sustainable Energy Department, TU Delft, The Netherlands. He previously held positions with Austrian Institute of Technology, Lawrence Berkeley National Laboratory, and the University of Pretoria. His research interests include intelligent power grids, integrated energy systems, the digitalization of energy processes, SCADA, cybersecurity, and hybrid energy system modeling and control. He is active in ISO, IEEE, and CEN standardization committees and serves as the Editor-in-Chief for *IEEE Industrial Electronics Magazine* and an Associate Editor for IEEE TRANSACTIONS ON INDUSTRIAL INFORMATICS.

ALEKSANDRA LEKIĆ (Senior Member, IEEE) received the B.S., M.S., and Ph.D. degrees in electrical engineering from the University of Belgrade, Serbia, in 2012, 2013, and 2017, respectively.

She was a Teaching Assistant and an Assistant Professor with the University of Belgrade and a Postdoctoral Researcher with KU Leuven and EnergyVille, Belgium. From 2020 to 2025, she was an Assistant Professor with TU Delft, where she is currently an Associate Professor. Her research focuses on circuit theory, control, and the stability analysis of nonlinear switching power converters and hybrid power systems with power electronics. She works on multiport power system analysis, HVDC systems, and harmonic stability assessment of hybrid systems combining passive and active components, including impedance-based MMC and other VSC models. Her work also includes developing nonlinear control algorithms based on Lyapunov theory and model predictive control methods for stable and efficient operation of switching converters and renewable-integrated power systems.